"THIS PDF IS AUTOMATICALLY GENERATED AND MAY HAVE FORMATTING ERRORS. THE AUTHOR-PROVIDED FILES ARE AVAILABLE IN THE MANUSCRIPT DOCUMENTS TAB."

Jupiter's interior and deep atmosphere: the first pole-to-pole pass with the Juno spacecraft

Authors: S. J. Bolton[1], A. Adriani[2], V. Adumitroaie[3], M. Allison[4], J. Anderson[1], S. Atreya[5], J. Bloxham[6], S. Brown[3], J. E.P. Connerney[7,8], E. DeJong[3], W. Folkner[3], D. Gautier[9], D. Grassi[2], S. Gulkis[3], T. Guillot[10], C. Hansen[11],W.B. Hubbard[12], L. Iess[13], A. Ingersoll[14], M. Janssen[3], J. Jorgensen[15], Y. Kaspi[16], S. M. Levin[3], C. Li[14], J. Lunine[17], Y. Miguel[10], A. Mura[2], G. Orton[3], T. Owen[18], M. Ravine[19], E. Smith[3], P. Steffes[20], E. Stone[14], D. Stevenson[14], R. Thorne[21], J. Waite[1]

Affiliations:

[1]Southwest Research Institute, San Antonio, TX, 78238, USA.

[2]Institute for Space Astrophysics and Planetology, National Institute for Astrophysics, Rome, 00133, Italy

[3]Jet Propulsion Laboratory, Pasadena, CA, 91109, USA.

[4]Goddard Institute for Space Studies, New York, New York, USA

[5]University of Michigan, Ann Arbor, MI, USA.

[6]Harvard University, Cambridge, MA, 02138

[7]Space Research Corporation, Annapolis, MD, 21403, USA.

[8]NASA Goddard Space Flight Center, Greenbelt, MD, 20771, USA.

[9]Laboratoire d'études spatiales et d'instrumentation en astrophysique, Observatoire de Paris, Meudon, 92195, France

[10]Université Côte d'Azur, Observatoire de la Côte d'Azur, Laboratoire Lagrange CNRS, Nice, 06304, France

[11]Planetary Science Institute, Tucson, AZ, 85719, USA

[12]Lunar and Planetary Laboratory, University of Arizona, Tucson, AZ 85721, USA

[13]Sapienza University of Rome, Rome, 00185, Italy

[14]California Institute of Technology, Pasadena, CA, 91125, USA

[15]National Space Institute, Technical University of Denmark, Kongens Lyngby, 2800, Denmark

[16]Department of Earth and Planetary Sciences, Weizmann Institute of Science, Rehovot, Israel, 76100

[17]Cornell University, Ithaca, NY, 14853, USA

[18]Institute for Astronomy, University, Honolulu, HI, 96822, USA

[19]Malin Space Science Systems, San Diego, CA, 92121, USA

[20]Center for Space Technology and Research, Georgia Institute of Technology, Atlanta, Georgia 30332, USA

[21]Department of Atmospheric and Oceanic Sciences, University of California-Los Angeles, Los Angeles, 90095, USA

*Correspondence to: sbolton@swri.edu

Abstract: On August 27, 2016, the Juno spacecraft acquired its first science observations of Jupiter, passing within 3000 km of the equatorial cloud tops. Images of Jupiter's poles show a chaotic scene unlike Saturn's poles. Microwave sounding reveals weather features down at least to 100 bars pressure, dominated by an ammonia-rich, narrow low-latitude plume resembling a deeper, wider version of Earth's Hadley cell. Near-infrared mapping reveals the relative humidity within prominent downwelling regions. Failure of the available interior models to reproduce Jupiter's gravity field has implications for the existence and mass of Jupiter's core. The observed magnetic field exhibits smaller spatial variations relative to that represented by low degree spherical harmonic models, indicative of a rich harmonic content.

One Sentence Summary: Juno's close pass by Jupiter provided close up views of Jupiter's turbulent polar atmosphere, the probing of Jupiter's deep atmosphere via microwave sounding, close up measurements of Jupiter's internal gravity and magnetic fields and a high resolution map of Jupiter's "hot spots".

Introduction

The primary science goal of Juno is the understanding of the origin and evolution of Jupiter, the history of our solar system and the more general theory of planetary system formation. To address these goals, Juno probes deep inside the cloud decks to constrain its interior structure using measurements of Jupiter's gravity and magnetic fields and deep atmospheric composition. Juno's elliptical orbit provides multiple periapsis passes very close to Jupiter, within 1.06 R_J of the Jovigraphic equator, on its pole-to-pole trajectory. A second science objective takes advantage of Juno's unprecedented close-in polar orbits to explore Jupiter's polar magnetosphere and intense aurorae *(1)*. Juno's suite of science instruments include an X-band and Ka-band communications subsystem for determining Jupiter's gravity field, dual magnetometers to map Jupiter's high order internal magnetic field (MAG), a set of six microwave radiometers operating between 1-50 cm wavelength to probe Jupiter's deep atmosphere (MWR), a visible color camera (JunoCam) and an infrared spectrometer and imager (JIRAM) to capture views of Jupiter. Juno also carries a suite of fields and particle instruments for in-situ sampling Jupiter's magnetosphere and investigating its powerful aurora *(1)*.

The Poles of Jupiter

The JunoCam instrument is a visible-light camera with blue, green, red and methane (centered at 890 nm) filters *(2)*. Figure 1 shows the first close-up 3-color images of the north and south poles of Jupiter, resolving details as small as 50 km as a result of the close proximity of Juno's orbits to the planet and their orientation over the poles. The wealth of detail in these images surpasses that of previous spacecraft because their trajectories were close to Jupiter's equatorial plane. Only

Pioneer 11 acquired non-oblique images over Jupiter's north pole but at ten times the distance of Juno *(3)*.

Within 30^{o} planetocentric latitude from each pole, the predominant zonal banded structure of lower latitudes breaks down. This boundary is coincident with a local drop in the zonal winds *(4,5)*. Within these polar regions, the banded structure is replaced by discrete features that are embedded in a background that is darker than anything at lower latitudes. The brightest features are ovals with external spiral-like extensions. A time-lapse sequence of the images reveals that the ovals are cyclones, that is, exhibiting counterclockwise motion about low pressure centers in the northern hemisphere. On this perijove, these types of ovals appear smaller in the north polar region than those in the south, with northern ovals covering a greater range of sizes, on the order of 1,400 km down to JunoCam's 50-km resolution limit. In the south they range from 200 to 1,000 km, and most lie between 71°S and 74°S (all latitudes in this report are planetocentric). The other bright regions in both hemispheres are amorphous. They resemble much smaller features at lower latitudes first identified in Voyager images as 'folded filaments' *(6)*, that are disorganized and turbulent with lifetimes of only about a day. In the north, the largest of these is on the order of 4,000-7,000 km in size. In the south, several are concentrated between 68°S and 73°S and stretch over 25° of longitude (10,000 km in size).

Jupiter's poles appear to be different from Saturn's in two specific ways. First, there is no equivalent to Saturn's north polar hexagon *(7)*, although circumpolar waves are observed *(8)*. Second is the lack of a vortex that is fast (150 m s^{-1}), compact (2° or 2500 km in radius), and centered on the pole similar to those at the north or south poles of Saturn *(9,10)*. Although the area within about 3^{o} of latitude around the north pole is unilluminated, the south pole is visible

and the features visible there are similar to others in the region. Thus the polar dynamics and structures of the atmospheres of these two planets are fundamentally different.

An unusual high-altitude cloud is visible past Jupiter's terminator near the top portion of the north polar image in Fig. 1. It is a roughly circular feature with a diameter of order 7,000 km. The effect of shadowing in Jupiter's clouds is evident. This cloud feature must be several scale heights (57 ± 21 km) above Jupiter's main polar cloud deck to be casting a shadow this far beyond the terminator. Juno cannot determine whether this is a towering cloud column whose base is shadowed or a detached high-altitude haze.

The Deep Atmosphere

The Juno Microwave Radiometer (MWR) measures thermal emission upwelling from previously unexplored depths in Jupiter's atmosphere *(11,12)*. Its two main scientific objectives are to determine the global abundance of ammonia and water and to observe dynamical features in the deep atmosphere. Most of our current knowledge of temperatures, winds, composition, and cloud properties is confined to the tops of the clouds, i.e., to pressures of 0.5 bar or less. The Galileo probe measured atmospheric properties down to the 22 bar level at one point on the planet, and therefore did not provide a global view *(13,14)*. In contrast, the MWR comprises six radiometric channels operating at wavelengths from 1.4 cm to 50-cm wavelength that collectively sample the thermal emission from pole to pole with better than 1° resolution in latitude at the equator, and from the cloud tops to pressures as deep as a few hundred bars.

During a perijove pass the MWR antennas scan north to south along the subspacecraft track as the spacecraft spins at 2 rpm along its orbit, obtaining overlapping measurements of the thermal

radiances of each point along the track at 100-msec intervals. The radiances are converted by Planck's law to a blackbody temperature and accordingly given in units of Kelvin *(15).* Further, the measurements have been corrected for finite beam effects to obtain source brightness temperature, or the effective mean radiance of Jupiter in the beam at the boresight axis, for each observation. The absolute accuracy of each measurement is 2% (uncorrelated among channels), while the relative accuracy at each wavelength is 0.1% *(16).*

Figure 2 shows plots of Jupiter's nadir brightness temperatures for all six channels, obtained during Juno's first two observational passes of Jupiter, occurring on Aug 27 (PJ1) and Dec 11, 2016 (PJ3). Only the nadir brightness is shown and used in the analysis in this paper, although the dependence of brightness on emission angle has been used to identify and eliminate data with suspected systematic errors. The brightness at each wavelength depends on the mean temperature of the atmosphere responsible for the emission, which in turn depends on the vertical distribution of opacity. The mean pressure sampled at each wavelength is indicated in the figure. Details of the radiative transfer calculations and the identification of systematic errors are given in the supplementary material. Brightness structure with latitude is observed at all wavelengths down to ~300 bars, but is seen predominately within 20° of the equator. Comparison of PJ1 and PJ3 brightness indicates that longitudinal variations are further confined to a "weather layer" at pressures less than about 9 bars. Strong correlations among wavelengths are observed in both passes near the region of the Equatorial Zone (EZ, ±5° latitude) and North Equatorial Belt (NEB, 5° to 20°) at all wavelengths. The repeatability of measured brightness at high latitudes and pressure depths > 10 bars demonstrates both that the atmosphere is stable in these regions and that the measurements are repeatable to at least the 1% level, or approximately the widths of the lines plotted in Fig. 2 (the small dip in the Ch 1 data for PJ3 at 40° N is due to contamination by

synchrotron emission). The relative structure—variation with latitude for each scan—is an order of magnitude better than the 1% repeatability variation.

We argue that the ~50 K variations of brightness temperature shown in Fig. 2 are due to variations of microwave opacity. If they were due to variations of temperature, the winds at the equator would be larger than those observed by at least an order of magnitude *(17)*. Ammonia is by far the dominant source of microwave opacity in Jupiter's molecular atmosphere, surpassing that of water vapor by more than an order of magnitude and all other sources by much more *(18)*. Therefore we solve for the ammonia distribution that best matches the observed brightness measurements from PJ1. In doing so, we assume that the sampled region is convective and transitions from a moist adiabatic lapse rate within the clouds to a dry adiabat below at a pressure that depends on atmospheric composition *(19)*. The results are shown in Fig. 3.

The features seen in Fig. 3 are both striking and unexpected. The dominant equatorial plume and the desiccated gas in the neighboring NEB, and the general depletion of ammonia at intermediate pressures at latitudes outside the equatorial plume resemble a giant Hadley cell extending out at least to ±40° latitude. However the ammonia crystals that fall out of the clouds evaporate before they reach the 1.5 bar pressure level. The structure is a Hadley cell without rain *(17)*. Traditionally, but based on marginal direct evidence, the ammonia has been assumed to be uniformly mixed below the clouds with perhaps a transition region from a few bars up to its saturation level *(20)*. The present results indicate that this is not the case, with the region of uniformly mixed ammonia confined to the region below 60 bars where it asymptotically approaches a level of 350 ppmv. We have examined modeling and experimental errors that impact our estimate, including 2% absolute uncertainties in measured brightnesses, H_2O concentration varying by a factor of ten relative to solar abundance, variations in the adiabat,

uncertainties in NH_3 opacity, and uncorrected sidelobe contributions. We arrive at a net uncertainty in the derived ammonia concentration of ±30 ppmv, while the depicted ammonia concentration is seen to vary by a factor of two, e.g., from 350 ppmv down to 175 ppmv. Possible causes for this structure and its implications for the general circulation of Jupiter's deep atmosphere are being studied *(17)* and will be discussed in future papers.

Hot Spots

The Jovian Infrared Auroral Mapper (JIRAM) provides infrared images and spectra of Jupiter's thermal emission *(21).* Using its dedicated imager channel on the M band (4.5-5.0 μm), JIRAM mapped Jupiter's upper troposphere. The coverage is almost complete between ±75° latitude. The map in Fig. 4 was obtained by superimposing about 1000 images with variable resolution (down to few tens of kilometers) taken during more than one day of observations. The mapping does not take into account the wind motion of the features, as adjacent zones are mapped one after the other, usually 30 seconds apart.

JIRAM geometric data are given in System III coordinate system. The brighter regions in Fig. 4 represent areas on Jupiter where thermal radiation escapes from pressure depths deeper than a few bars. These atmospheric emissions are mostly determined by reduced opacity of the widely-spread clouds. Such a low opacity allows to probe the composition of the troposphere below the reference level of 1 bar. Those "hot spots" are thought to be areas of downwelling and, hence, dry air. Many hot spots occur in a zone between 5° and 20° north latitude, the NEB, but "excess" thermal radiation is seen from much of the planet *(22,23).*

Mapping the water content inside hot spots to an unprecedented spatial resolution provides

information on the cycles of condensable species and cloud formation mechanisms. The hot spot where the water relative humidity has been retrieved and reported here can be seen in Fig. 4 at about 7°lat, 130°long. The retrieval code based on the preliminary results (22) has been developed and allows the reconstruction of the humidity. Results indicate a strong latitudinal dependence in the humidity distribution, a pattern that is recurrent in almost all hot spots investigated and suggests that inside the hot spot the relative humidity is lower than 3%. Results on the distribution of water and ammonia confirm a downwelling of the air in the center of the hot spot and upwelling on its edges. Values of water vapor relative humidity retrieved from the analysis of JIRAM data are typically between 5 and 8 times higher than the values previously reported *(24)* for the brightest parts of hot spots. These values remain rather small, however (below 10% in the entire area around the hot spot), confirming therefore the view of these structures as dry regions in the Jupiter atmosphere. Notably, analysis of two different hot spots from JIRAM data *(23)* clearly shows variable contents of water vapor between different hot spots. Consequently, while differences between our results and those previously reported *(24)* can be partially due to different retrieval methods (including adopted databases or the inclusion of a deep liquid water cloud), both analyses agree that hot spots vary over a wide range of relative humidity.

Gravity Field

The Jupiter gravity field was estimated from its effect on the Juno trajectory by measuring the Doppler shift of Juno's radio signal aquired by the NASA Deep Space Network (DSN). Juno's polar orbit and extremely low perijove make it is much more sensitive to Jupiter's gravity field than those of previous missions.

For the first science perijove (PJ1), the tracking station transmitted a signal at X-band (8 GHz). The spacecraft transponder coherently locked to this signal and transmitted signals back at X-band and Ka-band (32 GHz). With a low level of solar activity at that time, the dual-frequency downlink could be used to calibrate for the effects of charged particles in the Io plasma torus . We also have used data from the second perijove (PJ2) on October 19, 2016 when only X-band Doppler data was available.

The data were used to estimate the gravity field parameterized by zonal harmonics through degree 12 plus sectoral and tesseral harmonics of degree 2 along with corrections to the Jupiter spin axis direction. The Juno data have less sensitivity to the Jupiter mass parameter (GM) compared with the data from the Galileo orbiter flybys of the Galilean satellites. We have applied a constraint to the Jupiter GM based on that data. (25).

The estimated gravity harmonics are given in Table A3. The odd zonal parameters for degree greater than 3 along with J_{10} and J_{12} are not included in Table A3 since the estimated values are well below the uncertainties. The uncertainties account for both the effect of the observed data noise and from possible systematic errors. The consideration of previous analysis techniques (26) allows estimation of the uncertainty in parameters fit the observations due to parameters not well sampled by the data set. Our uncertainties include the effect of a possible gravity field of degree and order 30 due to surface winds with depth of 10,000 km that is not well sampled by data from two Juno orbits. (27) (See supplement for more details on the data noise and model used).

Table A3 also includes earlier gravity field estimates from Pioneer and Voyager (28) and from combination of the Pioneer and Voyager data with data from the Galileo mission (29) and also with data from the Cassini and New Horizons mission (30). These are associated with

ephemerides for the Jovian satellites designated Jup230 and Jup310. Unlike the Juno results presented here and the earlier Pioneer and Voyager analysis, the uncertainties for Jup230 and Jup310 do not account for possible systematic errors. The uncertainties for the Juno data ignoring systematic errors are about one order of magnitude smaller than the uncertainties given here. Aside from the differences in development of uncertainties, the estimated coefficients are generally in agreement within uncertainties. The uncertainty in J_4 and J_6, that are key parameters for constraining Jovian interior models, are improved with the Juno data over earlier estimates by factors of 5 and 22 respectively. The estimated J_4 and J_6 from the Jup310 solution are significantly different from the other solutions. This is thought to be due to systematic errors in photographic observations of Amalthea by Cassini and New Horizons.

Current published interior models do not agree precisely with the Juno data, although Nettelmann et al's model (31) is close because they were fitting JUP230 harmonics, a previous determination by Jacobson (29) that is also close to the Juno results. **Fig 5** shows that recent models, all of which have J_2 consistent with observation, show a significant scatter in J_4 and, to a lesser extent, in J_6. At the level of accuracy provided by the Juno measurements, differential rotation can affect these harmonics. We expect to get a better understanding of differential rotation by looking at small higher harmonics (e.g. J_8, J_{10}) and the odd harmonics that do not exist in hydrostatic equilibrium (e.g., J_3), The models have varying interior temperatures, heavy element distributions, and core masses. Some of the differences in predicted gravity arise from uncertainties in the equation of state for hydrogen-helium mixtures, the assumption of an adiabatic interior and the effects of helium immiscibility. Wahl et al (32) present a possible interpretation for the Juno data that requires a core that is dispersed out to perhaps as much as half the radius of Jupiter. An assessment of this and other possibilities must await additional Juno observations. The addition of heavy elements, in particular water, is important and we expect to

place constraints on this from the microwave observations. Magnetic field data may also reduce the ambiguity of interpretation.

Magnetic Field

Juno is the first spacecraft to venture so close to Jupiter's surface, passing to within 1.06 Rj of its center on its pole-to-pole trajectory. Juno's magnetometer (33) sampled at a rate of 64 vector samples/s throughout its closest approach, recording a magnetic field that greatly exceeded expectations based upon existing models (Figure 6). The maximum magnetic field observed during this periapsis was 7.766 Gauss, more than an order of magnitude greater than the Earth's maximum (south polar) surface field magnitude (0.66 G). The observed magnetic field displays more spatial variation relative to that represented by low degree and order spherical harmonic models, indicative of a rich harmonic content awaiting Juno's mapping phase. Juno's mapping phase designed to envelop Jupiter in a dense net of observations equally distributed in longitude, and will, based on this initial pass, undoubtedly reveal a field rich in higher harmonics.

While many spacecraft have sampled Jupiter's powerful magnetic field, none have sampled the field well inside of Io's orbit (5.95 Rj) since the Pioneer flybys (Pioneers 10 and 11) of the early 1970's. Our knowledge of Jupiter's magnetic field is thus limited by a paucity of direct observation close to the planet's surface, and reflected in spherical harmonic models (34, 35) that are confined to low degree and order, typically 3 or 4. The model field in widespread use and adopted by the Juno Project uses observations of the Io Flux Tube (IFT) footprint as an additional constraint, but even so, this model's degree and order 4 terms are only partially resolved. Figure 6 compares the observed field magnitude with that calculated from a suite of such models *(35)*, demonstrating that none adequately characterize the field near the surface.

Characterization of the field to high degree and order allows one to estimate the depth to the dynamo region, under the assumption that the harmonic spectrum is essentially "white" at the core surface – that is, represented by harmonic terms of equal amplitude by degree. The earth's dynamo radius (~.5 Re) may be located in this way and is consistent with seismic observations of the fluid core. The dynamo surface may also be located using the frozen flux theorem if variation of the magnetic field with time can be detected. The rich harmonic content indicated by Juno's very first (instrumented) periapsis pass portends a dynamo generation region not far beneath the surface. This may indicate that dynamo generation in Jupiter's interior – a process that requires electrically conducting fluid in convective motion – may occur in the molecular hydrogen layer above the pressure-induced transition to the metallic state as first suggested by Smoluchowski (36). Experimental data (37) indicate significant electrical conductivity in dense molecular hydrogen. Theoretical estimates consistent with these data (38) allow for a conductivity $\sigma \sim 1.5 \times 10^5$ S/m at $0.89R_J$ and 1.5×10^3 S/m at $0.93R_J$. These suggest a magnetic Reynolds number of $R_m \equiv \mu_o \sigma v L \sim 10^3$ to 10 for these radii, assuming a characteristic fluid velocity v~0.01m/s and characteristic length scale L~1000 km, both plausible choices for dynamo generation in Jupiter (39).

Summary

The surprising results presented here from Juno's first close passes of Jupiter are already rewriting of our understanding of this gas giant. The first direct glimpse of Jupiter's poles show no evidence of sustained dynamical features such as the hexagon encircling Saturn's pole. Instead Juno found numerous cyclonic storms and a storm illuminated in Jupiter's nightside that provided a measurement of its vertical extent. The first deep microwave sounding of Jupiter demonstrates the power of this technique unveiling spatial and time structure in the ammonia

abundance never previously seen or contemplated. The initial measurement of Jupiter's gravity requires new interior models with possible implications for the existence and mass of Jupiter's core. The magnitude of the observed magnetic field observed was 7.766 Gauss, almost twice as strong as expected. More results from Juno's first pass are discussed in a companion paper (1). During the course of next few years, Juno will provide a wealth of data from over 32 passes equally close to Jupiter, but at diverse set of longitudes, effectively mapping the planet.

References and Notes

1. Connerney et al., *Science,* this issue

2. C. J. Hansen et al., *Space Sci. Rev.* doi10.007/s/11214-014-0079-x (2016).

3. T. Gehrels, in *Jupiter: Studies of the interior, atmosphere, magnetosphere and satellites,* T. Gehrels, Ed. (U. Arizona Press. Tucson, 1976) pp. 531-563.

4. E. Garcia-Melendo, A. Sanchez-Lavega, *Icarus 152,* 316-330 (2001).

5. X. S. Asay-Davis, P. S. Marcus, M. H. Wong, I. de Pater, *Icarus 211*, 1215-1232 (2011).

6. A. P. Ingersoll et al. *Nature* 280, 773-775 (1979).

7. D. A. Godfrey, *Icarus* 76, 335-356 (1988).

8. N. Barrado-Izagirre, S. Perez-Hoyos, A. Sanchez-Lavega, *Icarus 202,* 181-196 (2009).

9. A. Antuñano, T. Río-Gazelurrutia, A. Sánchez-Lavega, R. Hueso, *J. Geophys. Res*. 129, 155-176 (2015).

10. U. A. Dyudina et al., *Icarus* 202, 240-248 (2009).

11. M. A. Janssen et al., *Icarus* 173, 447-453 (2005).

12. M. A. Janssen et al., *Space Sci. Rev*. in press (2017).

13. W. M. Folkner, R. Woo, S. Nandi, *J. of Geophys. Res.-Planets* 103, 22847-22855 (1998).

14. M. H. Wong, P. R. Mahaffy, S. K. Atreya, H. B. Niemann, T. C. Owen, *Icarus* 171, 153-170 (2004).

15. M.A. Janssen, editor, *Atmospheric Remote Sensing by Microwave Radiometry*, (Wiley & Sons, New York, 1993).

16. S.T. Brown, M.A. Janssen, S. Misra, submitted to *Geophys. Res. Lett.* (2017).

17. A.P. Ingersoll, C. Li, M. A. Janssen, submitted to *Geophys. Res. Lett.* (2017).

18. P.G. Steffes et al., *Space Sci. Rev.* doi: 10.1007/s11214-01600265-0 (2017).

19. C. Li, A.P. Ingersoll, F. Oyafuso, S. Ewald, M.A. Janssen, submitted to *Geophys. Res. Lett.* (2017).

20. S. K. Atreya et al., *Planet. Space Sci.* 53, 498-507 (2005).

21. A. Adriani et al., *Space Sci. Rev*., doi:10.1007/s11214-014-0094-y (2014).

22. G. Sindoni et al., Submitted to *Geophys. Res. Lett.* (2017).

23. D. Grassi et al., Submitted to *Geophys. Res. Lett.* (2017).

24. M. Roos-Serote et al., *Planet. Space Sci*. 52, 397-414 (2004).

25. R. Jacobson, R. Haw, T. McElrath, P. Antreasian, *Advances in the Astronautical Sciences*, 103, 465-486 (1999*).*

26. G. J. Bierman, *Factorization methods for discrete sequential estimation (Dover Publications, Mineola, New York, 2006).*

27. M. Parisi, E. Galanti, S. Finocchiaro, L. Iess, Y. Kaspi, *Icarus* 267, 232-242 (2016).

28. J. K. Campbell, S. P. Synnott, Astrophys. J. 90, 364–372 (1985).

29. The JUP230 solution corresponds to the gravity field of Jupiter calculated by R.A. Jacobson in 2003 using Pioneer, Voyager and Galileo data as released on http://ssd.jpl.nasa.gov/?gravity_fields_op

30. The JUP310 solution corresponds to the gravity field of Jupiter calculated by R.A. Jacobson in 2013 using Pioneer, Voyager, Galileo and New Horizons data as released on http://ssd.jpl.nasa.gov/?gravity_fields_op

31. N. Nettelmann, A. Becker, B. Holst, R. Redmer, *Astrophysical Journal* 750 DOI:10.1088/0004-637X/750/1/51(2012).

32. Wahl, et al., submitted to *Geophys. Res. Lett.* (2017).

33. Connerney, J. E. P., Benn, M., Bjarno, J. B., Denver, T., Espley, J., Jorgensen, J. L., Jorgensen, P. S., Lawton, P., Malinnikova, A., Merayo, J. M., Murphy, S., Odom, J., Oliversen, R., Schnurr, R., Sheppard, D., Smith, E. J. (2017) The Juno Magnetic Field Investigation, *Space Sci. Rev.*, doi: 10.1007/s11214-017-0334-z.

34. Connerney, J.E.P., Açuna, M.H., Ness N.F., & Satoh, T. (1998). New models of Jupiter's magnetic field constrained by the Io Flux Tube footprint. *J. Geophys. Res., 103,* 11929 -11939.

35. Connerney, J.E.P. (2015). Planetary magnetism. Volume 10: Planets and Satellites. In G. Schubert and T. Spohn, (Eds.) *Treatise in Geophysics*, Elsevier, Oxford, UK, vol. 10.06, 195-237. ISBN: 978-0-444-63803-1.

36. . R. Smoluchowski, *Astrophysical Journal Letters* 200, 119-121 (1975).

37.. W. J. Nellis, S. T. Weir, A. C. Mitchell, *Science* 273, 936-938 (1996).

38. M. French, A. Becker, W. Lorenzen, N. Nettelmann, M. Bethkenhagen, J. Wicht, R. Redmer, *Astrophysical Journal Supplement* 202, doi: *10.1088/0067-0049/202/1/5* (2012).

39. T. Guillot, D. J. Stevenson, W. B. Hubbard, D. Saumon, in *Jupiter,* F. Bagenal, T. Dowling, W.B. McKinnon Eds. (Cambridge University Press, New York, 2004), chap. 3.

40. Miguel, Y., Guillot, T. Fayon, L. (2016) Astronomy and Astrophysics vol 596 , A114 DOI: 10.1051/0004-6361/201629732

41. T. R. Hanley, P. G. Steffes, B. M. Karpowicz, A new model of the hydrogen and helium-broadened microwave opacity of ammonia based on extensive laboratory measurements. *Icarus* 202, 316-335 (2009).

42. K. Devaraj, P. G. Steffes, D. Duong, The centimeter-wavelength opacity of ammonia under deep jovian conditions. *Icarus* 241, 165-179 (2014).

43. A. Bellotti, P.G. Steffes, G. Chinsomboon, Laboratory measurements of the 5-20 cm wavelength opacity of ammonia, water vapor and methane under simulated conditions for the deep jovian atmosphere. *Icarus* 280, 255-267 (2016).

44. E.C. Morris, R. W. Parsons, Microwave absorption by gas mixtures at pressures up to several hundred bars. I. Experimental technique and results, *Australian Journal of Physics*, 23, 335-349 (1971).

45. Asmar, S. W., Armstrong, J. W., Iess, L., & Tortora, P. (2005), Spacecraft Doppler tracking: Noise budget and accuracy achievable in precision radio science observations. *Radio Science*, *40*, doi:10.1029/2004RS003101.

46. Atkinson, D. H., Pollack, J. B., & Seiff, A. (1998), The Galileo probe Doppler wind experiment: Measurement of the deep zonal winds on Jupiter. *J. Geophys. Res. Planets*, *103*, 22911-22928.

47. Barnes, J.A., Chi, A.R., Cutler, L.S., Healey, D.J., Leeson, D.B., McGunigal, T.E., Mullen, J.A., Smith, W.L., Sydnor, R.L., Vessot, R.F. and Winkler, G.M., (1971), Characterization of frequency stability. *IEEE transactions on instrumentation and measurement*, *1001*, 105-120.

48. Bierman, G., (1997), Factorization methods for discrete sequential estimation, Academic Press, New York.

49. Bird, M. K., Asmar, S. W., Brenkle, J. P., Edenhofer, P., Funke, O., Pätzold, M., & Volland, H., (1992), Ulysses radio occultation observations of the Io plasma torus during the Jupiter encounter. *Science*, *257*, 1531-1535.

50. Eshleman, V. R., Tyler, G. L., Wood, G. E., Lindal, G. F., Anderson, J. D., Levy, G. S., & Croft, T. A. (1979). Radio science with Voyager at Jupiter: Initial Voyager 2 results and a Voyager 1 measure of the Io torus. *Science*, *206*, 959-962.

51. Gavrilov, S. V., & Zharkov, V. N. (1977). Love numbers of the giant planets. *Icarus*, *32*, 443-449.

52. Jacobson, R., Haw, R., McElrath, T., & Antreasian, P. (1999). A comprehensive orbit reconstruction for the Galileo prime mission in the J2000 system, Advances in the Astronautical Sciences, 103, 465-486.

53. Kaula, W. M. (1966), *Theory of satellite geodesy: applications of satellites to geodesy*, Blasidell Pub. Co., Waltham, Mass.

54. Milani, A., & Gronchi, G. (2010). *Theory of orbit determination*. Cambridge University

Press.

55. Parisi, M., Galanti, E., Finocchiaro, S., Iess, L., & Kaspi, Y. (2016). Probing the depth of Jupiter's Great Red Spot with the Juno gravity experiment. *Icarus*, *267*, 232-242.

Acknowledgements

Figure 1 images were processed by citizen scientist Roman Tkachenko (as part of Juno's outreach program). The visible map shown in Figure 2 is based on observations made with the NASA/ESA Hubble Space Telescope under program GO14334, the Outer Planet Atmospheric Legacy Program, OPAL (See [MWR-14]). A.P.I, X.Y.Z, and U.V.W. acknowledge financial support from the Juno project of NASA. T.G. and Y.M. acknowledge financial support from CNES. Support for the HST program was provided by NASA through a grant from the Space Telescope Science Institute, which is operated by the Association of Universities for Research in Astronomy, Inc., under NASA contract NAS5-26555. All maps from this program can be retrieved at: https://archive.stsci.edu/prepds/opal/.

Figure Captions

Fig. 1. Orthographic projection of JunoCam color-composite images of the north and south polar regions of Jupiter obtained August 27, 2016. The north polar image was taken at 11:59 UT when the spacecraft was 73,009 km from Jupiter's cloud deck, and the south polar image was taken at 13:56 UT when the spacecraft was 95,096 km from the cloud deck.

Fig. 2. Nadir brightness temperatures in the six channels of the MWR vs. planetocentric latitude. The black and green curves are from the perijove passes on August 27, 2016 and December 11, 2016, for which the closest approaches were at 13:44 UTC and 17.05 UTC, respectively. The corresponding longitudes at equator crossing were 264°W and 7°W (System III). The frequencies of channels 1-6 are 0.6, 1.2, 2.6, 5.2, 10, and 22 GHz, respectively. Brightness temperature in Kelvins is given on the left. Estimates of the pressure where the physical temperature is equal to the average brightness temperature are given below each curve. Underlying the plots of brightness temperature is a section of a Jupiter map taken by HST on February 10, 2016, in the visible wavelength range (PIA19643). The latitude of the bands has not changed during the months between the two data sets, but the longitudes of individual features have changed beyond the limits of the image. The white circles indicate the footprint sizes for channels 3-6, for which the full width at half power is 12° (these are shown sparse for illustration, but the observations are in fact continuous in latitude). Channels 1 and 2 have full width at half power of 20°. The footprint size reflects the changing altitude of the spacecraft during its ~1-hour pass above the planet from north to south.

Fig.3. Planetocentric latitude-altitude cross-section of ammonia mixing ratio in units of parts per million by volume (ppmv). The thin blue band at the top—near the 1-bar level—is where ammonia is condensing and the mixing ratio is low (<100 ppmv). The high mixing ratio at the equator is interpreted as air that is exchanging with the deep atmosphere at pressures of 100 bars or more where the mixing ratio is 330-370 ppm.

Fig. 4. Cylindrical map of the infrared emission from Jupiter as detected by JIRAM. The map is colored according to radiance in W m^{-2} sr^{-1} integrated from 4.5 to 5.0 μm. System III reference frame is used.

Fig. 5. J_4 and J_6 pre-Juno observed values by Campbell & Synnott (1985) (brown), by Jacobson (2003) (JUP230, black), and Jacobson (2013) (JUP310, purple) compared to Juno's preliminary measurement (red). Models available from the literature are also shown; these models are described in ref 40.

Fig. 6. Magnitude of the magnetic field observed along Juno's closest approach trajectory (solid line) as a function of time and spacecraft latitude, compared with that computed from a suite of existing models (35). The stippled region illustrates the range of such model predicts, bounded by the VIP4 model beneath and the GSFC O4 model above.

"Figure #1"

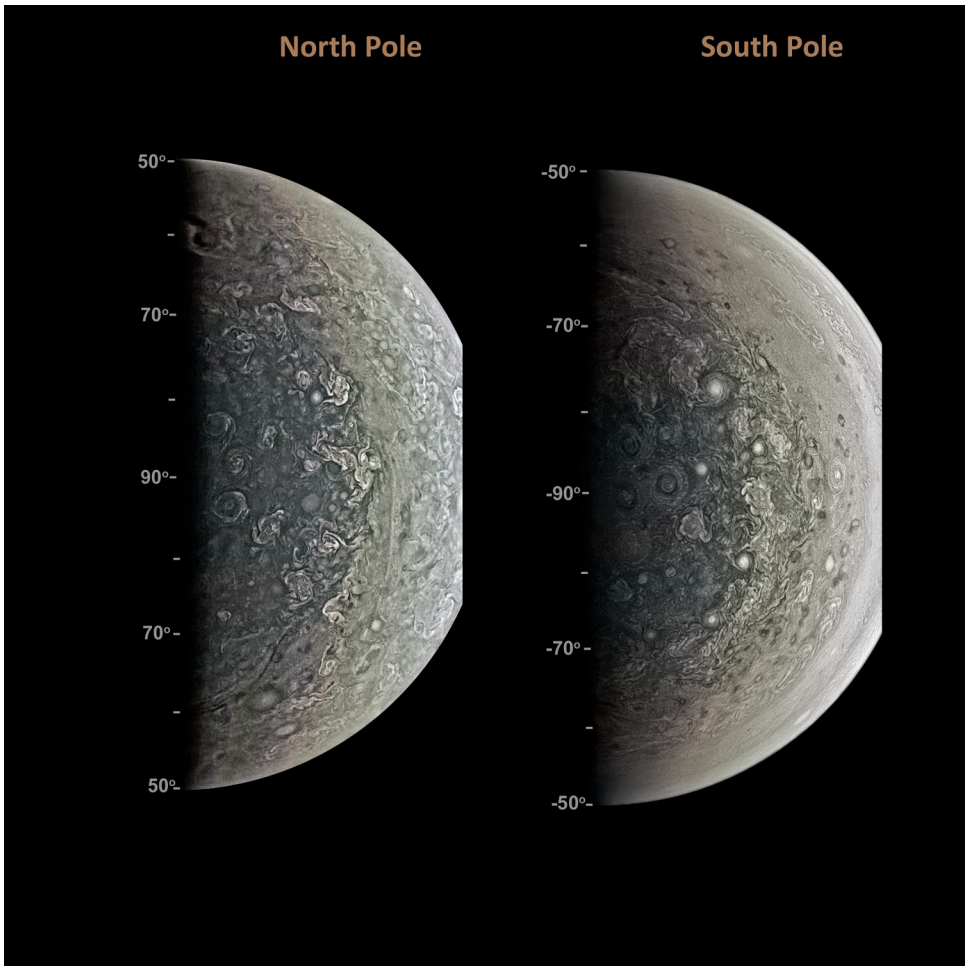

"Figure #2"

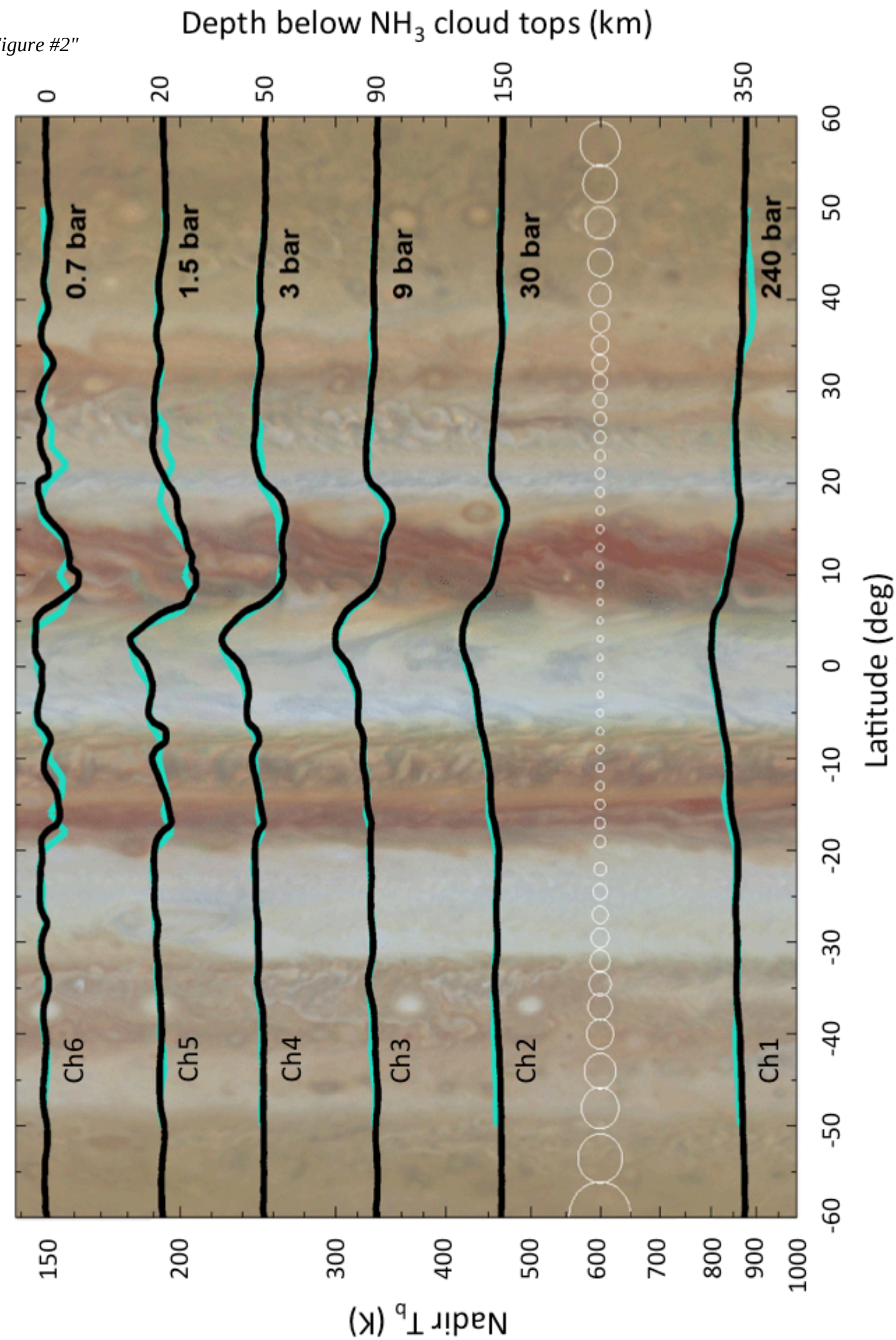
Depth below NH3 cloud tops (km)
0
20
50
90
150
350
0.7 bar
1.5 bar
3 bar
9 bar
30 bar
240 bar
Ch6
Ch5
Ch4
Ch3
Ch2
Ch1
Nadir Tb (K)
150
200
300
400
500
600
700
800
900
1000
Latitude (deg)
-60
-50
-40
-30
-20
-10
0
10
20
30
40
50
60

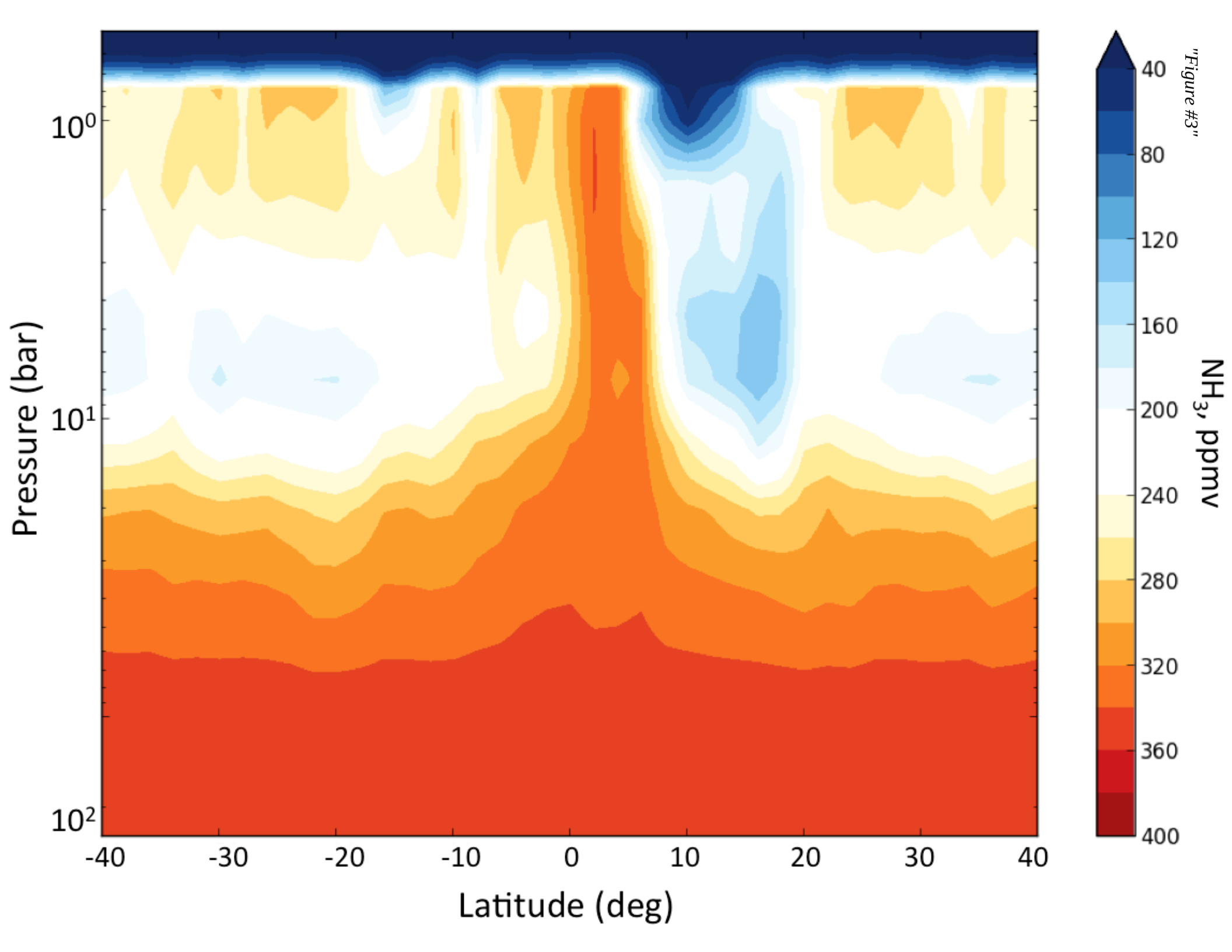
"Figure #3"
Pressure (bar)
10^0
10^1
10^2
-40
-30
-20
-10
0
10
20
30
40
Latitude (deg)
40
80
120
160
200
240
280
320
360
400
NH_3, ppmv

"Figure #4"

radiance (W / sr / m²)
2
1
0
180
90
0
-90
-180
longitude
75
60
45
30
15
0
-15
-30
-45
-60
-75
latitude

"Figure #5"

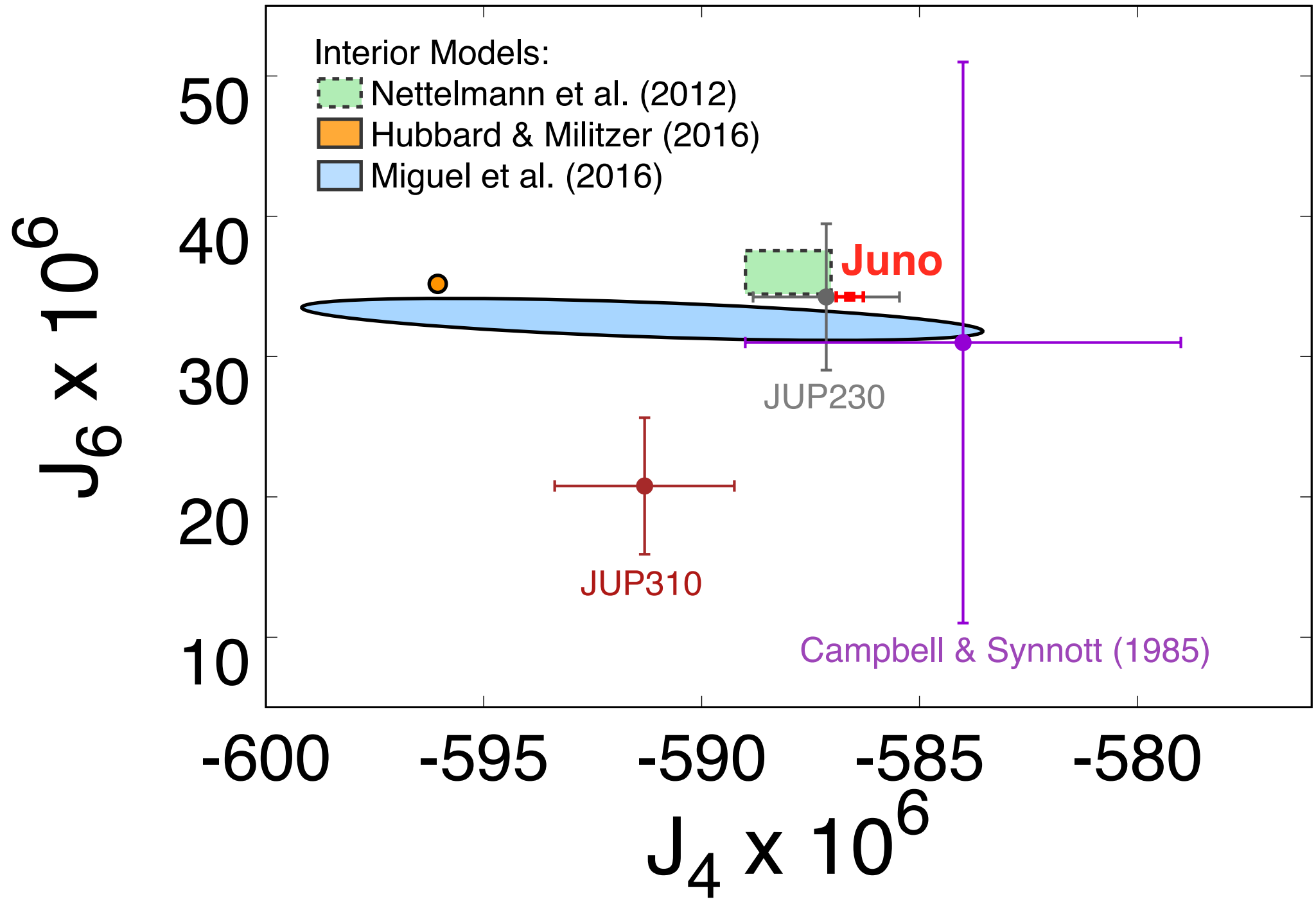
Interior Models:
Nettelmann et al. (2012)
Hubbard & Militzer (2016)
Miguel et al. (2016)
Juno
JUP230
JUP310
Campbell & Synnott (1985)
50
40
30
20
10
-600
-595
-590
-585
-580
J6 x 10^6
J4 x 10^6

"Figure #6"

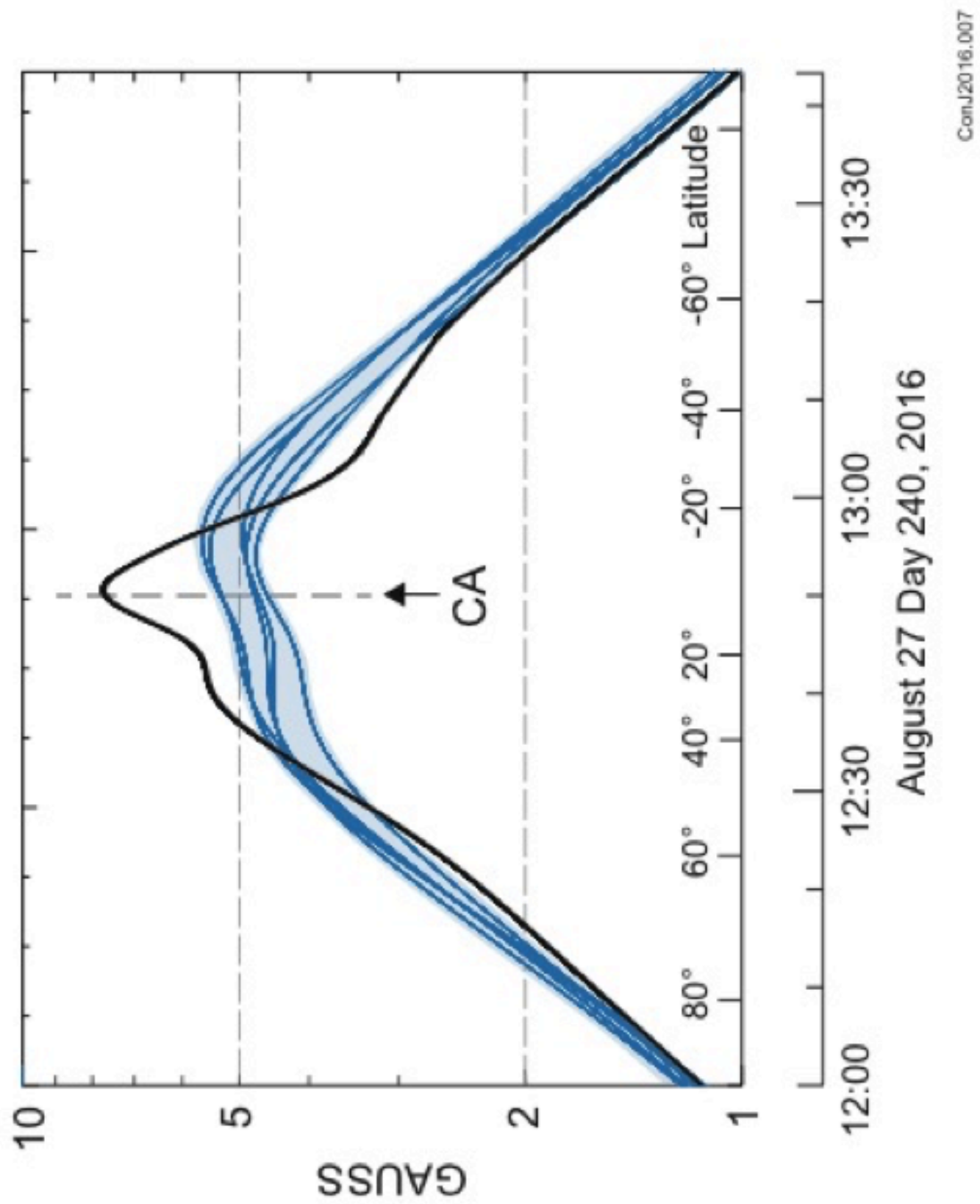
GAUSS
10
5
2
1
CA
80°
60°
40°
20°
-20°
-40°
-60° Latitude
12:00
12:30
13:00
13:30
August 27 Day 240, 2016
ConJ2016.007

MWR Science paper Supplementary Material

The Juno Microwave Radiometer (MWR) comprises six separate radiometers (channels 1-6) that operate at frequencies distributed approximately by octave from 600 MHz to 22 GHz (50 to 1.2 cm wavelength) respectively, as listed in Table A1. Each channel obtains contiguous measurements of the antenna temperature T_a at 100-ms intervals with the uncertainties given in the table. Since the spacecraft spins at 2 rpm, observations are taken at spacecraft clock angle increments of 1.2°. Noting the antenna beamwidths in the table, this amounts to 10 or more observations per MWR footprint on Jupiter. Allowing for averaging of adjacent measurements and the typical source temperature at each wavelength, the intrinsic instrument noise in the nadir brightness temperatures shown in Fig. 2 is are negligible compared to the relative and absolute errors of 0.1% and 2% respectively.

Table A1. MWR Characteristics

Channel	Frequency [GHz]	Wavelength [cm]	Beamwidth [deg]	ΔT_{noise} (100 ms) [K]
1	0.600	50	20.6°	0.59
2	1.248	24	21.0°	0.54
3	2.597	11.55	12.1°	0.42
4	5.215	5.75	12.1°	0.39
5	10.004	3.0	12.0°	0.21
6	21.900	1.37	10.8°	0.19

At the longest-wavelength channels, particularly channel 1, the synchrotron emission becomes particularly strong and contamination of Jupiter measurements due to radiation from this source entering the antenna sidelobes must be dealt with. Particular care in the design and implementation of the antennas was taken to minimize this source of error so that it does not limit our ability to measure the nadir brightness and its emission angle dependence. Figure A1 shows a validation of the design using data obtained during the PJ1 pass. This plot shows the calibrated antenna temperature obtained as a function of spacecraft clock angle with respect to nadir for channel 1, showing the emission from both sources in context. Each horizontal line in the figure represents the contiguous antenna temperature measurements obtained during one rotation of the spacecraft as it sweeps from north to south across Jupiter, crossing closest to nadir at 0° clock angle, then sweeping around across the radiation belt in the opposite hemisphere. The vertical shape symmetric about t0 clock angle is Jupiter's thermal emission, while the bright signal in the rest of the sky is the synchrotron emission. The spurs of synchrotron radiation that begin to impinge on the planet near ±40° latitudes correspond to the north and south horns of radiation from mirror-point electrons that come close to the spacecraft these latitudes. The separation of thermal atmospheric radiation from synchrotron emission appears complete in this image, although detailed calculations using the known antenna beam pattern show that a small contribution from the latter remains at the nadir line (42). Nevertheless this contributes less than 1% to the atmospheric signal and is negligible for the nadir brightness analysis reported here, although the effect on emission angle dependence remains to be dealt with in future work. The rapid decrease of the synchrotron emission with decreasing wavelength makes it negligible for nadir emissions in all other channels.

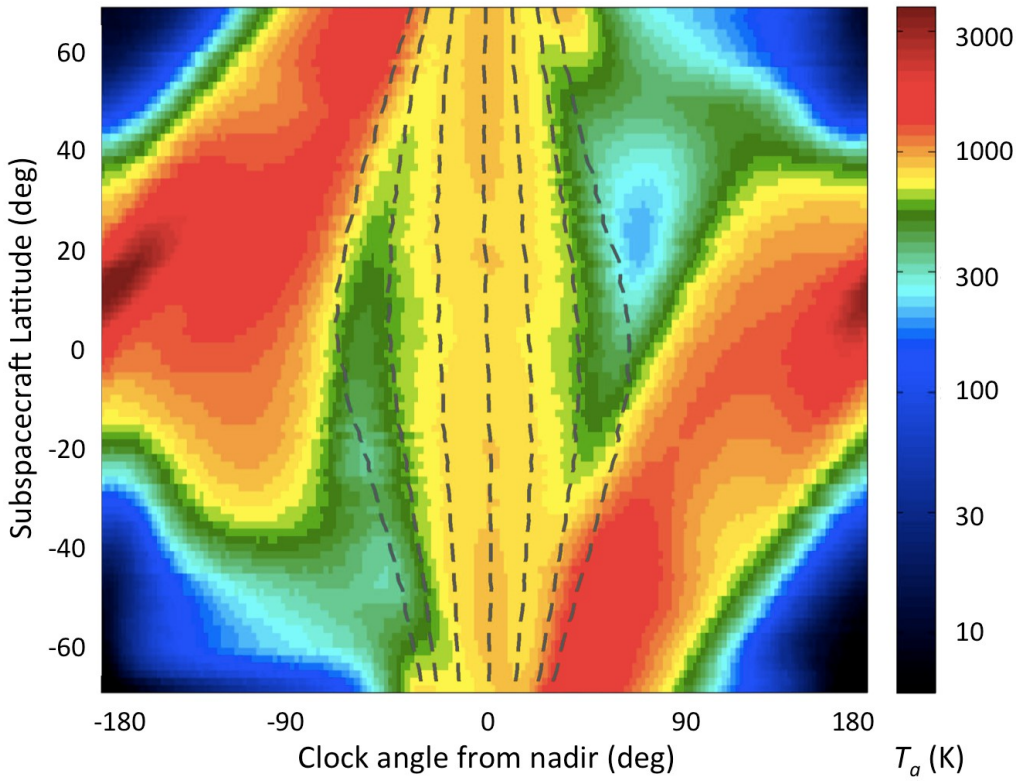

Fig. A1: Channel 1 antenna temperature as a function of spacecraft clock angle through the perijove 1 pass. The dashed lines indicate lines of constant incidence angle at 0, 30, 60 and 90 degrees.

The calculations used to interpret the measurements make use of the Juno Atmospheric Microwave Radiative Transfer (JAMRT) code developed by the Juno project for this purpose (42). Combined with a model of the atmosphere, JAMRT computes radiances from profiles of temperature, ammonia and water from the cloud tops down to pressures of 1000 bars. The model uses experimental data on the opacity of ammonia and water in hydrogen-helium mixtures at temperatures up to 600 K and pressures up to 100 bars (20, 41-43). The uncertainties of the opacity models have been determined to be about 5% to 7% from low pressures up to 100 bars. These determinations are supplemented by room-temperature data that range to several hundred bars (44). The model allows for variations in pressure-temperature structure, variable concentrations of constituents in addition to water and ammonia gas that affect the opacity such as water/ammonia cloud droplets and NH_4SH (from H_2S reacting with NH_3). All brightnesses are computed assuming a one-dimensional line-of-sight integration from above the atmosphere with no scattering or refraction.

Figure A2 shows the brightness temperature contribution functions computed for the six MWR channels using JAMRT and an assumed atmosphere containing nominal concentrations of ammonia and water (3 x solar each), each assumed to be uniformly mixed up to their respective saturation levels and following a saturation curve above that. The contribution function is calculated here as the fractional contribution to the net brightness temperature per increment of log (P), so that the area under the curve for a given pressure range is proportional to the net thermal contribution from that range. Observe that the contribution functions are approximately symmetric in log (P) for channels 2 through 6 (24 to 1.37 cm), with peaks around 30, 10, 3.5, 1.5 and 0.7 bars respectively, and are generally contained within the region where the opacities of

NH_3 and H_2O have been measured. The highest frequency lies in the center of the strong ammonia 1-cm band, and the remaining frequencies were chosen to provide overlapping weighting functions descending as far as feasible into Jupiter's depths. However, most of the contribution to channel 1 brightness temperatures depends on extrapolation by as much as two orders of magnitude in pressure beyond the range of laboratory measurements, and to temperatures in excess of 2000 K. While structure seen at this lowest frequency is very important, its interpretation will have a different character than that from the other channels because the deep opacity is more uncertain.

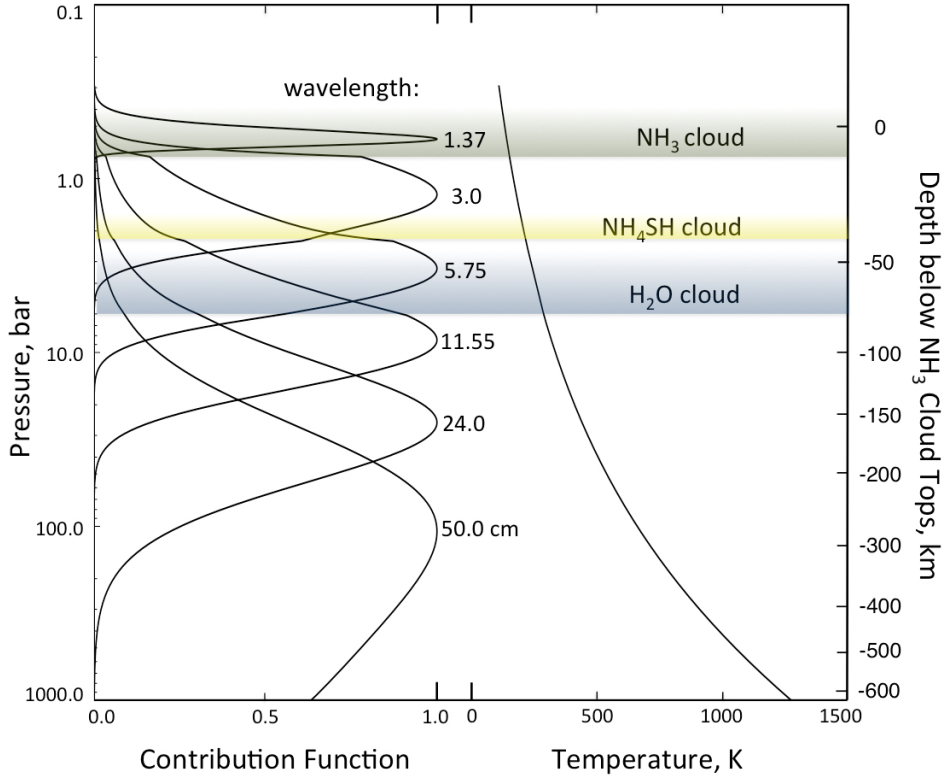

Fig. A2: Contribution functions for a nominal Jovian atmosphere at the MWR wavelengths and points for laboratory measurements of NH_3 and H_2O microwave opacity in context with a Jovian pressure-temperature profile.

Comparison of PJ1 and PJ3 brightnesses indicates that longitudinal variations are further confined to a "weather layer" at pressures less than about 9 bars, consistent with VLA observations.
The results are qualitatively consistent with the Galileo probe results, which have low values of the ammonia mixing ratio extending well below the ammonia cloud and then transitioning to a higher value deeper down. Figure 3 shows the transition occurring at a pressure of ~25 bar, but this is deeper by a factor of 3 in pressure than that observed by the Galileo probe. Juno's value for the NH_3 mixing ratio at 200 bars is 330-370 ppmv, whereas absorption of the Galileo probe radio signal gives 700±100 ppmv, and the Galileo probe mass spectrometer gives 568±215 ppmv (one has to convert from numbers relative to H_2 to numbers relative to the bulk mixture). The unexpected concentrations measured by the Galileo probe for both NH_3 and H_2O have been ascribed to its landing in an anomalous atmospheric region (a 5-micron hot spot). In the context of our results, we note that the probe descended into the atmosphere at 7° N just at the transition between the equatorial plume and the NEB ammonia-dry region, where the measurements would be expected to depend strongly on the exact location. It is argued by Ingersoll et al. (17) that this general location is a region of intermixed ascending ammonia-rich and descending ammonia-poor

gas, and a single measurement cannot be expected to give a representative picture of Jupiter's composition for condensable gasses.

Gravity Field Supplement

Mission orbit geometry and data

Key geometry information for the first two Juno perijoves following orbit insertion, designated PJ1 and PJ2, are given in Table A2. The orbit was nearly polar with orbit period 53 days. The time of perijove is given in barycentric dynamical time (TDB). The orbit plane was nearly perpendicular to the direction from Earth to Jupiter. Both perijoves were near solar conjunction. At perijove the height of the spacecraft above the 1-bar ellipsoid was about 4100 km at latitude 3.8° N and 4.7° N. The spacecraft was nearly over the north pole of Jupiter about one hour before perijove and above the south pole about one hour after perijove. When above the north and south poles the spacecraft was approximately one Jupiter radius above the 1-bar level.

Table A2. Geometry information for perijoves 1 and 2, including time of perijove, one-way light time LT from spacecraft to Earth, distance d from Juno to Earth, inclination of orbit plane to Jupiter equator, height above Jupiter 1-bar ellipsoid at perijove, latitude λ of perijove, angle β between orbit normal and direction from Earth to Jupiter, and angular separation SEP between Sun and Jupiter as seen from Earth.

PJ	Time (TDB)	LT(min)	d(au)	i(°)	h(km)	λ(°)	β(°)	SEP(°)
1	08/27/2016 12:51:52	53.0	6.37	89.9	4147	3.8	2.8	22.6
2	10/19/2016 18:12:02	53.1	6.39	90.0	4179	4.7	9.4	18.2

For PJ1 the data used cover from 3.2 hours before perijove to 5.1 hours after perijove. For PJ2 the data covered from 3.1 hours before perijove to 2.8 hours after perijove. For both perijoves, the tracking station transmitted a radio signal to the spacecraft at X-band (8 GHz). A transponder on the spacecraft locked coherently in phase onto the signal from the tracking station and transmitted a signal back to the tracking station.

For PJ1 the spacecraft transmitted signals at both X-band and at Ka band (32 GHz). The difference in the Doppler shift of the X-band and Ka-band signals were used to calibrate the effect of charged particles on the radio signal from the spacecraft to Earth. The only significant signature in this calibration is near the time of closest approach to Jupiter. Near perijove the spacecraft was inside the orbit of Io and the radio signal passed through the Io plasma torus. The Io plasma torus causes an effect on radio signals that has been previously measured from the Voyager and Ulysses spacecraft (45, 46). We used the dual-frequency radio signal to Earth to calibrate the effect of the plasma torus, also applied, appropriately scaled, to the X-band radio signal from the tracking station to the spacecraft. We applied an estimate of the effect of the Io plasma torus to the PJ2 data based on the dual-frequency measurements from PJ1.

The data noise for PJ1 was dominated by a combination of fluctuations in the troposphere and antenna mechanical noise. The data noise for PJ2 was dominated by solar plasma but at lower level than expected (47). The measurement noise for the two orbits is characterized by the Allan deviation (48) that measures the fractional frequency stability as a function of the integration time. For the Jovian gravity field estimation the main time scales of interest are from ~100 s to ~1000 s, for which the change in Doppler is caused by the zonal gravity harmonics from degree 2 to degree 12. Figures A3 and A4 show the Allan deviation for Doppler residuals. These are based on residuals after estimation of the relevant parameters. Data from the hour centered on perijove are excluded, since over that time the estimated parameters can absorb some of the measurement noise. The slope of the Allan deviation for PJ1 residuals over 100 s to 1000 s indicates white frequency noise, while for PJ2 the slope of Allan deviation indicates noise dominated by solar plasma. For PJ1 the slope of the Allan deviation indicates the Doppler measurements as a function of time are uncorrelated, while for PJ2 the Doppler measurements at different times have non-zero correlation as a function of the time between point. This correlation function can be calculated to provide the correct data weighting to use for estimation.

Gravity model and estimation technique

The mass distribution of a planet is generally different from that of a homogeneous spherical body. For this reason, the external gravitational potential of Jupiter can be conveniently expanded in series of spherical harmonics of degree *l* and order *m* (49):

$$U(r,\lambda,\phi)=\frac{GM}{r}\sum_{n=0}^{\infty}\sum_{m=0}^{n}\left(\frac{R}{r}\right)^{n}P_{nm}(\sin\phi)\left[C_{nm}\cos(m\lambda)+S_{nm}\sin(m\lambda)\right],$$

where G is the gravitational constant, M and R are the mass and radius of Jupiter, r is the distance from Jupiter's center of mass, ϕ is the latitude, λ is the longitude, P_{nm} are the un-normalized associated Legendre functions, and C_{nm} and S_{nm} are the un-normalized spherical harmonic coefficients. The gravitational acceleration affecting the trajectory of Juno while orbiting about Jupiter can be calculated by taking the gradient of the gravitational potential. In turn, spherical harmonics can be estimated by precise Doppler tracking of the spacecraft along with other relevant parameters.

The state vector x is the set of the estimated parameters. By means of radiometric observables z, it is possible to obtain a least-squares estimate x_c of the state vector, designed to combine a priori information and new data [*Bierman*, 1977]:

$$x_c=\left(A^T WA+\tilde{\Lambda}\right)^{-1}\left(A^T Wz+\tilde{\Lambda}\tilde{x}\right) \quad ,$$

where A is the matrix of observation partials, W is the observable weighting matrix, $\tilde{\Lambda}$ is the a priori information matrix and $\tilde{x}$ is an unbiased *a priori* estimate of the state vector. The quantity $P_{x,}$ given by:

$$P_x = \left(A^T W A + \tilde{\Lambda} \right)^{-1} \quad ,$$

is the covariance matrix, which bears information about the estimation accuracies. The square roots of the diagonal elements correspond to the formal uncertainties on the estimated parameters.

The measurements used for gravity analysis allow the estimation of a limited number of parameters, supported by the available data strength. However, unestimated parameters (for instance higher degree and order gravity harmonics) can be dynamically correlated with the estimated parameters and might undermine the filter accuracy and confidence in the estimated values and covariance.

One strategy to prevent the underestimation of the covariance is the technique of consider analysis. This approach features a set of parameters y which are not estimated, but whose a priori covariance P_y is used to augment the least-squares uncertainty. The consider covariance P_{CON} is given by:

$$P_{CON} = P_x + S P_y S^T \quad ,$$

where S is the sensitivity matrix:

$$S = \partial \left(x - x_c \right) / \partial y$$

where $x - x_c$ is the difference between the true value of x and the least-squares estimate x_c . The consider covariance is composed of two positive definite terms: (i) the standard covariance matrix P_x ; (ii) an additional component which depends on the sensitivity matrix and the a priori covariance for the consider parameters.

When data is accumulated (i.e. data available for more than one perijove) it is possible to adopt a multi-arc approach (50), where the information from different arcs is combined. In this case, the formal uncertainties P_x will decrease because of the higher information content, while consider covariance P_{CON} can sometimes increase when estimated parameters are highly correlated with unestimated parameters.

Jovian gravity field estimation

The Doppler data from PJ1 and PJ2 were used to estimate the Jovian gravity field parameterized by zonal harmonics through degree 12 plus sectoral and tesseral harmonics of degree 2 along with corrections to the Jupiter spin axis direction and the initial position and velocity of the spacecraft for each perijove. The Juno data have less sensitivity to the Jupiter mass parameter (GM) than the data from the Galileo orbiter flybys of the Galilean satellites. We have applied a constraint to the Jupiter GM based on a fit to the Galileo orbiter data. (51). The a priori uncertainties for the other estimated parameters were set to be large compared with the final estimated uncertainties. The Jovian gravity field is also affected by tides raised by the Jovian satellites, with largest contribution by Io. Because the longitude of Juno with respect to Io was almost the same for PJ1 and PJ2 the data are not able to separate tide signature. Instead we have modeled the effect of tides using a

value for the k_2 Love number of 0.379 from *Gavrilov and Zharkov* (52). The estimated gravity coefficients include the average effect of the tides.

The estimated gravity parameters are given in Table A2. The correlations between parameters are given in Table A3. The odd zonal parameters for degree greater than 3 along with J10 and J12 are not included in Table 2 since the estimated values are well below the uncertainties. The uncertainties listed account for both the effect of the observed data noise and from possible systematic errors using the consider analysis described above. The uncertainties include the effect of consider parameters describing a possible gravity field of degree and order 30 due to surface winds with depth of 10,000 km (53). This results in gravity coefficient uncertainties that are fairly conservative but not an upper bound. The winds speeds used for this model are observed at the could tops, while to deeper winds may be larger. The only observation of Jovian wind speeds below the cloud levels from the Galileo probe were significantly larger than the cloud-top winds (54).

The estimated values of the degree two sectoral and tesseral coefficients are well below the uncertainties. The values of C_{21} and S_{21} are zero if Jupiter's principal axis of inertia coincides with the spin axis. The values of C_{22} and S_{22} are zero if the mass distribution is symmetric about the rotation axis. These properties are expected for the fluid planet in equilibrium and have been used as constraints in some earlier analyses. The Juno data are strong enough to confirm these expectations.

Table A3. Estimated Jovian gravity field parameters Pioneer/Voyager and from Juno's first two science orbits in combination. The zonal harmonics J_n and degree-2 tesseral harmonics $S_{i,j}$ and $C_{i,j}$ are unnormalized and dimensionless. The Jupiter spin axis direction given by right ascension α and declination δ 2000.0. The gravity harmonics from Pioneer and Voyager have been scaled from the Jupiter radius they used to the radius 71492 km used by Juno and their pole direction converted from Earth-Mean-Equator of 1950 to Earth-Mean-Equator of 2000.

Parameter	Pioneer/Voyager	Jup230	Jup310	Juno PJ1&PJ2
GM(km^3/s^2)	126686537.5 ± 101	126686534.9 ± 1.5	126686534.2 ± 2.7	126686533.0 ± 2.0
J_2 x10^6	14697.3 ± 1	14696.43 ± 0.21	14695.62 ± 0.29	14696.514 ± 0.272
J_3 x10^6	1.4 ± 5	−0.64 ± 0.90		−0.067 ± 0.458
J_4 x10^6	−583.9 ± 5	−587.14 ± 1.68	−591.31 ± 2.06	−586.623 ± 0.363
J_6 x10^6	30.8 ± 20	34.25 ± 5.22	20.78 ± 4.87	34.244 ± 0.236
J_8 x10^6				−2.502 ± 0.311
C_{21} x10^6				0.026 ± 0.303
S_{21} x10^6				0.030 ± 0.368
C_{22} x10^6	−0.030 ± 0.150	0.007 ± 0.008	−0.010 ± 0.067	0.005 ± 0.170
S_{22} x10^6	−0.007 ± 0.150	−0.013 ± 0.009	−0.014 ± 0.061	−0.010 ± 0.214
α (deg)	268.058 ± 0.005	268.0566 ± 0.0002	268.0571 ± 0.0003	268.057 ± 0.002
δ (deg)	64.494 ± 0.002	64.4953 ± 0.0001	64.4958 ± 0.0001	64.496 ± 0.013

Table A4. Correlation matrix for estimated Jovian gravity field parameters. The correlation matrix is symmetric so only the upper diagonal is shown. The diagonal elements of the matrix are the parameter uncertainties.

	GM5	RA0	DEC0	C21	S21
GM5	2.00E+00	−1.50E−03	5.53E−03	3.74E−04	−7.78E−03
RA0		3.96E−05	−8.28E−01	−9.82E−01	2.67E−01
DEC0			2.21E−04	7.31E−01	−7.57E−01
C21				2.35E−07	−1.26E−01
S21					2.85E−07

	S21	C22	S22	J2	J3
GM5	−7.78E−03	−6.69E−03	−5.62E−03	−3.14E−03	5.61E−03
RA0	2.67E−01	6.75E−01	8.32E−01	3.47E−01	−5.07E−01
DEC0	−7.57E−01	−9.61E−01	−9.95E−01	−4.77E−01	7.57E−01
C21	−1.26E−01	−5.65E−01	−7.35E−01	−3.45E−01	4.44E−01
S21	2.85E−07	8.74E−01	7.48E−01	3.80E−01	−7.62E−01
C22		2.64E−07	9.48E−01	5.00E−01	−8.32E−01
S22			3.31E−07	4.72E−01	−7.51E−01
J2				1.22E−07	−3.21E−01
J3					1.73E−07

	J4	J6	J8
GM5	2.94E−03	4.22E−03	3.93E−03
RA0	−5.73E−01	−5.77E−01	−6.29E−01
DEC0	5.70E−01	6.67E−01	6.87E−01
C21	5.17E−01	4.84E−01	5.47E−01
S21	−3.62E−01	−5.14E−01	−4.85E−01
C22	−5.14E−01	−6.24E−01	−6.31E−01
S22	−6.18E−01	−7.13E−01	−7.30E−01
J2	−3.16E−01	−3.17E−01	−3.45E−01
J3	3.90E−01	4.23E−01	4.47E−01

J4	*1.21E-07*	*8.33E-01*	*8.63E-01*
J6		*6.54E-08*	*9.27E-01*
J8			*7.55E-08*

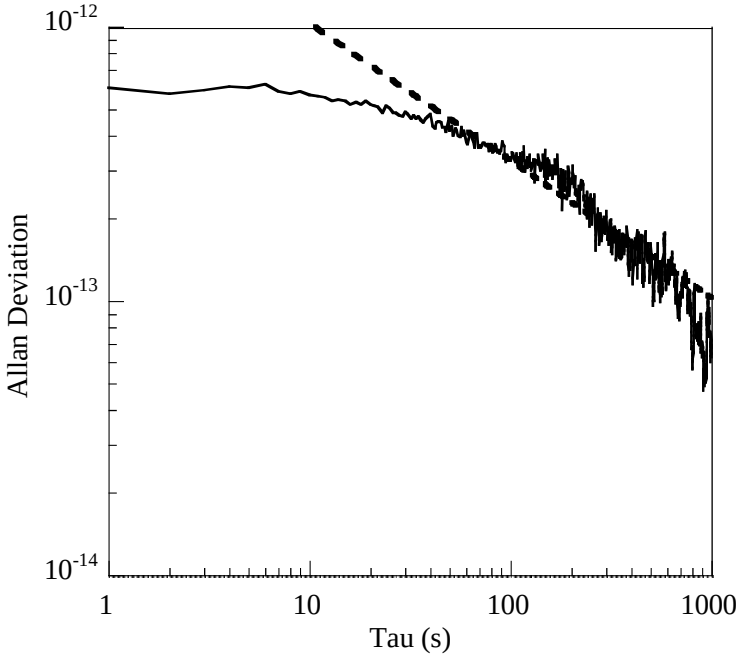

Figure A3. The Allan deviation of the Doppler measurements from PJ1. For time scales from 100 to 1000 seconds the slope is approximately proportional to $tau^{-1/2}$ (dashed line) indicating the Doppler measurements are independent for those time scale.

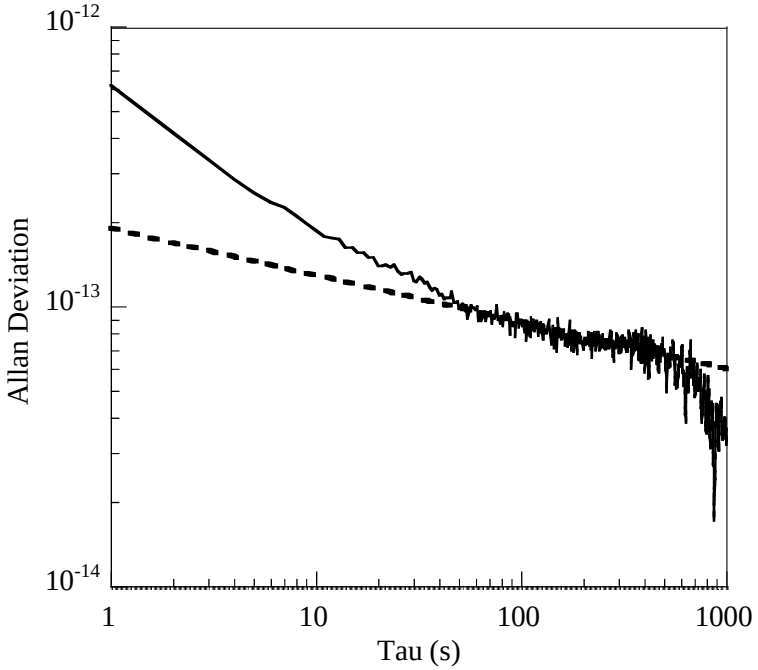

Figure A4. The Allan deviation of the Doppler measurements from PJ2. For time scales from 100 to 1000 seconds the slope is approximately proportional to $tau^{-1/6}$ (dashed line) indicating the Doppler measurements are correlated on those time scales due to the character of solar plasma.